Paper F

Deposition of Green House Gases by Compositional Simulator: Long Term Reactive Transport of CO_2 in the Sand of Utsira

Khattri, S.K.
Hellevang, H.
Fladmark, G.E.
Kvamme, B.

Submitted to *Transport in Porous Media*

Deposition of Green House Gases by Compositional Simulator: Long Term Reactive Transport of CO_2 in the Sand of Utsira

*S. K. Khattri, **H. Hellevang, *G. E. Fladmark and **B. Kvamme

*Department of Mathematics University of Bergen Norway**
*Department of Physics & Technology University of Bergen Norway***
e–mail: sanjay@mi.uib.no

Abstract

Carbon Dioxide (CO_2) released during fossil fuel consumption is a major source of greenhouse gases. Geological storage of CO_2 is a strategy to reduce emissions of CO_2 into the atmosphere. For the success of safe deposition of CO_2 into geological formations, it is required to understand the detailed behaviour pattern of CO_2 dynamics. For this purpose, we have developed a reactive fluid flow and geochemical transport numerical model for predicting long-term disposal of green house gases in geological formations. The model is based on a compositional reservoir simulator in which mineral and chemical reactions are integrated. The model consists of fifteen chemical species and sixteen mineral species.

We are also simulating two scenarios with and without regional flow. We analyze impact of fluid movement on long term CO_2 migration at the Utsira. Here, we analyze how flow of medium fluids affects important parameters such as the pH and evolution of CO_2 saturation. The input data for the simulations has similarity with the CO_2 storage facility at the Sleipner Vest field in the Norwegian sector of the North Sea. For example, the injection rate, injection period, properties of sand and shale layers.

In this work, we present the mathematical models and their discretization for capturing major physical processes associated with CO_2 sequestration/deposition in a porous medium. We verify our simulator by comparing our results against available results.

Key words: CO_2 sequestration/deposition; Utsira formation; Compositional simulation; Multi phase flow; Multi component flow; Porous media; Reactive Transport.

Table 1
Estimate of storage capacities for different geological trap types [20].

Storage Option	Global Capacity (Gt. [gigatons] CO_2)
Depleted gas fields	690
Depleted oil fields/CO2-EOR	120
Deep saline aquifers	400 - 10 000
Unminable coal seams	40

1 Introduction

There is a wider acceptance among scientific community that emission of greenhouse gases into the atmosphere is causing global warming and changing our climate (see [11–15, and references therein]). Carbon dioxide (CO_2) represents approximately 60% [16] of all the green house gases generated globally and it is responsible for nearly 64% of the enhanced green-house effect [16]. Sequestration/deposition of CO_2 in underground formations is one potential option for reducing the CO_2 emissions to the atmosphere. CO_2 can be deposited in depleted oil and gas fields, coal mines and deep saline aquifers. Table 1 reports estimates of storage capacities for different geological formations [20]. Our work is concerned with storage of CO_2 in deep saline formations; e.g. the Utsira formation. It is the first industrial-scale underground CO_2 storage site [17] and it is located at the Sleipner Vest field in the Norwegian sector of the North Sea. Approximately 1,000,000 tonnes/year of CO_2 is injected into the sands of the Utsira formation [2]. CO_2 injection was started in October 1996 and it is planned to continue for about twenty years [12,2]. Carbon-dioxide is injected at an approximate depth of 1000 m below the sea level. Approximate temperature and pressure at the point of injection are 37°C and 10 MPa respectively. Under these temperature and pressure conditions carbon-dioxide is super-critical with a density of about 700 $\mathrm{kg\,m^{-3}}$. Thus, carbon-dioxide at the point of injection has density of a fluid, but the compressibility of a gas. 3-D seismic data suggests that the Utsira formation contains several shale or clayey layers and the these layers follow the topography of the top surface [17–19]. The Utsira sand is overlain by a thick overburden which is primarly shale and it forms part of the Mio-Pliocene Utsira formation (see [21,22]).

There are essentially three main trapping mechanisms related to deposition of carbon dioxide in aquifers. These are hydrodynamic trapping, solubility trapping and mineral trapping. Hydrodynamic trapping is essentially a feature of the flow through the system as given by convection and diffusion governed mass transport through the specific porous media. Solubility trapping can be defined as dissolution of CO_2 in the formation water. CO_2 can react directly or indirectly with the minerals present in the medium leading to the precip-

itation of the secondary carbonates. It is referred as mineral trapping and is the most desired form of trapping CO_2 because of long timescales. Mineral trapping can retain CO_2 for long period of time. During mineral trapping, the corresponding reactions from CO_2 over to bicarbonate and carbonate are fast and in most realistic reservoir simulations these reactions can be considered as instant. Rates of dissolution of minerals varies significantly. It can be a few days to several years, depending on the mineral species. Typically the dissolution rate is few days for calcium carbonate in sour environment close to the injection zone and up to several hundred years for silicates. Dissolved ions from the minerals will be transported through the reservoir and may eventually precipitate as solid minerals again in other parts of the reservoir where pH is higher.

For the success of deposition, it is required to understand the detailed behaviour pattern of CO_2 dynamics in porous medium. Numerical simulations have been used in the past for understanding migration of hydrocarbons in reservoirs. Mathematical modelling and numerical simulations are an ideal approach for understanding the future of CO_2 in geological formations. Numerical modelling can play an important role in evaluating the feasibility and reliability of a formation for CO_2 disposal.

Deposition of CO_2 in porous media is reactive transport of multi-phase and multi-component system. Moreover, studies of reactive transport of multi-component and multi-phase system in a porous medium are mixture of many sciences. Reactive transport of multi-component and multi-phase system involves physical and chemical processes. Physical processes can be convection and diffusion of species. Chemical processes can be reaction of species with each other, with the medium fluids and with the solid minerals. Such reactive transport can be described by coupled non-linear system of partial differential equations (PDEs). These PDEs can be solved numerically for capturing the physics and chemistry of the underlying phenomenon. Numerical simulation of such a phenomenon is a challenging task because of the underlying non-linear mathematics, coupled physical and chemical processes, complicated geometry of the formations, complex distribution of geological properties (permeability, porosity) etc. These equations have been implemented in the in-house research simulator named Athena. Athena is solving these PDEs by the compositional simulation techniques. Compositional simulation techniques have been extensively used in the past for describing flow of hydrocarbons in reservoirs (see [5–7, and references therein]). For a detailed description of the discretization methods and solvers in the Athena, interested readers are referred to [3–9,30,29].

For handling chemical and mineral reactions, we have developed a package named ACCRETE [31]. It is coupled with the Athena simulator.

An outline of the article is as follows. In Section 2, equations for CO_2 flow in porous medium are derived. Section 3 presents discretization of the continuum equations. Thermodynamics of single phase and two phase systems is mentioned in the Section 4. In the Section 5, a brief introduction to the geochemistry is presented. Section 6 presents a verification of the code. Section 7 presents two simulations of realistic scenarios. Finally Section 8 concludes the article.

2 Continuum Equations of CO_2 Flow in Porous Medium

In this section, we derive continuum equations for CO_2 dynamics in a porous medium. For notational convenience, the subindices are used for denoting components and the subindices are used for denoting phases. System consists of two phases: water phase (w) and gas phase (g). Let there be total n_ν components distributed in-between these two phases. These components can be water, carbon-dioxide, sodium chloride, various kinds of chemicals, etc. The primary variables are temperature T, pressure P and molar masses N_ν of each of the components ν. Our task in this section is to form partial differential equations for these primary variables. Secondary variables like molar mass of component ν in phase l (N_ν^l) can be expressed in terms of the primary variables.

For performing numerical simulation, the geological formation is divided into smaller elements called finite volumes or cells. Let us consider a finite volume with a volume V and with boundary S. We are assuming that the shape of the finite volumes are not changing with time. The geological formation is composed of these finite volumes. Each of the volume V has unique medium properties such as porosity, permeability, etc. In a finite volume all the phases can be present.

2.1 The Mass Conservation Equation

A mass balance equation for a component ν in a finite volume with volume V and surface S is written as follows

$$\frac{\partial}{\partial t}\left(\int_V m_\nu\right) + \int_V (\nabla \cdot \mathbf{m}_\nu) = \int_V q_\nu, \tag{1}$$

where the sub-script V on the integral sign indicates that it is a volume integral, m_ν denotes the moles per unit volume (molar mass density) of the component ν, $\mathbf{m}_\nu$ is the molar mass flux and q_ν denotes the number of moles of ν that are generating or disappearing per unit volume per unit time.

Since the component ν can be in any of the phases (water and gas), the molar mass flux of component ν is given as

$$\mathbf{m}_\nu = \sum_{l=w,g} C_\nu^l \, \xi^l \, \mathbf{v}^l, \tag{2}$$

where l denotes either the water or gas phase, C_ν^l denotes the mass fraction of the component ν present in the phase l, ξ^l is the molar density of phase l and $\mathbf{v}^l$ is the Darcy velocity of the phase l. Molar mass density of the component ν is given as

$$m_\nu = \phi_p \sum_{l=w,g} C_\nu^l \, S^l \, \xi^l. \tag{3}$$

Here ϕ_p is the porosity of the finite volume V (the fraction of the void space in the total volume of the porous medium. It is a property of the medium), S^l is the saturation of the phase l. It should be noted that the porosity can change due to mineral reactions. For simplicity, we consider only incompressible rock; i.e., porosity does not depend on the pressure. The total mass N_ν of a component ν in a finite volume V is

$$N_\nu = \int_V m_\nu. \tag{4}$$

The total source or sink of a component ν in a finite volume V is

$$Q_\nu = \int_V q_\nu. \tag{5}$$

2.2 The Water Pressure Equation

Since water pressure is one of the primary variables, an equation for water pressure is required. Which is constructed using the method of Volume Balance. For a detailed description of the method, see the Reference [25]. Let us define the difference R between the pore volume V_p and volume of all phases as

$$R = V_p - \sum_{l=w,g} V^l, \tag{6}$$

This difference is a function of the water pressure P^w, the overburden pressure W and molar mass of each component N_ν; i.e., $R = R(P^w, W, N_\nu)$. According to the Volume Balance method, the difference between the pore volume and the volume of all phases has to be zero at all time. Linearising the difference

R by the Taylor Series in time

$$R(t + \Delta t) = R(t) + \frac{\partial R}{\partial t}\,\Delta t, \tag{7}$$

putting the term $R(t+\Delta t)$ equal to zero and using chain rule, $(\partial R/\partial t)$ results in

$$\frac{\partial R}{\partial P^w}\,\frac{\partial P^w}{\partial t} + \sum_{i=1}^{n_c} \frac{\partial R}{\partial N_i}\,\frac{\partial N_i}{\partial t} = -\frac{R}{\Delta t} - \frac{\partial R}{\partial W}\,\frac{\partial W}{\partial t}. \tag{8}$$

This is the equation for the water pressure, which is parabolic in nature. The gas phase (CO_2) pressure is given in terms of the water phase pressure and the capillary pressure as

$$P^{CO_2} = P^{H_2O} + P_c^{wg} \quad \text{or} \quad (P^g = P^w + P_c^{wg}). \tag{9}$$

Here P_c^{wg} is the capillary pressure between the water and the gas phases.

2.3 The Temperature Equation

For deriving the temperature equation, we are using the following energy conservation equation for a control volume V

$$\frac{\partial}{\partial t}\int_V \rho\, u - \int_S k\,\nabla T = -\int_S h\,\rho\,\mathbf{u} + \int_V q, \tag{10}$$

where $\rho\, u$ represents the total internal energy density and $h\,\rho\,\mathbf{u}$ represents the convective flux term. These terms are given as

$$\rho\, u = \sum_{l=w,g} \phi_p S^l u^l \rho^l + u_r \rho_r\,(1-\phi_p), \tag{11}$$

$$h\,\rho\,\mathbf{u} = \sum_{l=w,g} h^l \rho^l \mathbf{v^l}. \tag{12}$$

Here k is the bulk heat conductivity, ρ_r is the mass density of the rock, u_r is the internal energy of the rock, u^l is the internal energy density of the phase l and h^l is the enthalpy of the phase l.

3 Discretization of the Continuum Equations

3.1 Discretization of Molar Mass Equation

Here we derive an implicit formulation of the mass transport equation (1) [26–28, and references therein]. After substituting relations (2), (3), (4) and (5) in the equation (1) results in

$$\frac{\partial N_\nu}{\partial t} + \int_V \sum_{l=w,g} \nabla \cdot \left(C_\nu^l \, \xi^l \, \mathbf{v}^l \right) \quad = Q_\nu, \tag{13}$$

The total molar mass of a phase l is given as $N^l = V^l \, \xi^l$. Let the specific volume of the phase l be a^l ($a^l = 1/V^l$). Substituting ξ^l and V^l in the above equation

$$\frac{\partial N_\nu}{\partial t} + \int_V \sum_{l=w,g} \nabla \cdot \left(C_\nu^l \, a^l \, N^l \, \mathbf{v}^l \right) = Q_\nu, \tag{14}$$

Applying the divergence theorem to the second term in the above equation and substituting the molar mass of component ν in the phase l ($N_\nu^l = C_\nu^l \, N^l$) reads

$$\frac{\partial N_\nu}{\partial t} + \int_S \sum_{l=w,g} \left(N_\nu^l \, a^l \, \mathbf{v}^l \right) \cdot \hat{\mathbf{n}} \quad = Q_\nu, \tag{15}$$

where $\hat{\mathbf{n}}$ is the unit normal to the surface S. Let the boundary surface S be composed of small surfaces S_i such that $\cup S_i = S$ and $S_i \cap S_j = 0$ if $i \neq j$.

Space discretization of the equation (15) is done by Cell Centered Finite Difference approximation method and the continuity of the flux term is enforced on the interfaces. A discrete form of the surface integral in the equation (15) is

$$\int_S \sum_{l=w,g} \left(N_\nu^l \, a^l \, \mathbf{v}^l \right) \cdot \hat{\mathbf{n}} \approx \sum_{S_i} \sum_{l=w,g} \left(N_\nu^l \, a^l \right)_{[\text{in}]} \theta_i^l, \tag{16}$$

In the above equation, $\theta_i^l = (\mathbf{v}^l \cdot \hat{\mathbf{n}})_i \, A_i$. Here A_i is the surface area of the interface S_i. The subindex in denotes the upstream control volume with respect to the interface S_i of the control volume V. Substituting equation (16) in the equation (15) results in

$$\frac{\partial N_\nu}{\partial t} + \sum_i \sum_{l=w,g} \left(N_\nu^l \, a^l \right)_{[\text{in}]} \theta_i^l = Q_\nu, \tag{17}$$

In the above equation, the convective part θ_i^l, the specific phase volume a^l and Q_ν are computed at the time t^n while N_ν^l is computed at time t^{n+1}.

Time discretization in the above equation is done by the Backward Euler approximation

$$\frac{[N_\nu]^{n+1} - [N_\nu]^n}{\Delta t^n} + \sum_{S_i} \sum_{l=w,g} \left(\left[N_\nu^l\right]^{n+1} \left[a^l\right]^n \right)_{[\text{in}]} \left[\theta_i^l\right]^n = [Q_\nu]^n \,, \tag{18}$$

In the above equation, N_ν is the primary variable and N_ν^l is the secondary variable. We need to express secondary variables in terms of primary variables. N_ν^l is a function of the molar masses of individual components (the primary variables N_ν); i.e., $N_\nu^l = N_\nu^l(N_1, N_2, \ldots)$. Linearising the molar mass of component ν in the phase l in terms of molar masses of species by the Taylor series

$$\left[N_\nu^{l[k+1]}\right]^n = \left[N_\nu^{l[k]}\right]^n + \sum_\mu \left[\left(\frac{\partial N_\nu^l}{\partial N_\mu} \right)^{[k]} \right]^n [\Delta N_\mu]^n \,, \tag{19}$$

In the above equation, the summation is over all the components n_c, $[k]$ is the point about which Taylor series was expanded to get the value at the point $[k+1]$ and $[\Delta N_\mu]^n = \left[N_\mu^{[k+1]}\right]^n - \left[N_\mu^{[k]}\right]^n$. To simplify, we are ignoring the cross-derivative terms in the equation (19). The assumption of negligible cross-derivatives between different components eliminates the coupling and makes it possible to achieve greater computer efficiency by sequential solution [3,4]. Thus, considering

$$\frac{\partial N_\nu^l}{\partial N_\mu} = 0 \quad \text{if} \quad \nu \neq \mu, \tag{20}$$

in the equation (19), we get

$$\left[N_\nu^{l[k+1]}\right]^n = \left[N_\nu^{l[k]}\right]^n + \left[\left(\frac{\partial N_\nu^l}{\partial N_\nu} \right)^{[k]} \right]^n [\Delta N_\nu]^n \,, \tag{21}$$

Substituting the above relation into the equation (18) results in the following Newton Iteration

$$\boldsymbol{J} \left[\Delta {N_\nu}^{[k]}\right]^n = \beta_\nu, \tag{22}$$

$$N_\nu^{k+1} = N_\nu^k + \Delta {N_\nu}^{[k]} \quad k = 0, 1, \ldots. \tag{23}$$

Here $N_\nu^0 = [N_\nu]^n$. The Jacobian and right hand side are given as

$$\boldsymbol{J} = \left[\frac{\boldsymbol{I}}{\Delta t} + \left(\sum_{S_i} \sum_{l=w,g} \left(\frac{\partial N_\nu^l}{\partial N_\nu} \right) \left[a^l\right]^n [\theta_i^l]^n \right)_{[\text{in}]} \right]^k, \tag{24}$$

$$\beta_\nu = Q_\nu - \left(\frac{[N_\nu^k]^n - [N_\nu]^n}{\Delta t^n} \right) - \sum_{S_i} \sum_{l=w,g} \left[N_\nu^{l[k]} a^l\right]_{[\text{in}]}^n [\theta_i^l]^n. \tag{25}$$

After sufficient number of iterations; i.e., when $k \rightarrow \infty$ then $N_\nu^{k+1} \rightarrow [N_\nu]^{n+1}$.

3.2 Discretization of the Temperature Equation

The conductive term in the heat flow equation (10) is approximated by the Two Point Flux Approximation (TPFA) [24] as follows

$$\int_S k\,\nabla T = \sum_m \int_{S_m} k\,\nabla T \approx \sum_m \sum_j \xi_{ij}\,(T_j - T_i), \tag{26}$$

where the index j means a control volume with a temperature T_j sharing the interface S_m. S_m is the m^{th} part of the surface boundary S. ξ_{ij} is the conductivity coupling coefficient of the two control volumes i and j sharing the interface S_m. T_i is the temperature of the finite volume V. The source term in the equation (10) is treated explicitly for each control volume

$$\int_V q \approx Q, \tag{27}$$

The convective flux in the heat flow equation (10) is small compared to the conductive flux. So it can be neglected or can be treated explicitly. For explicit treatment, the Darcy velocity at the boundary surfaces are approximated by the value at the upstream control volume. Thus, the convective flux term is discretized as

$$\int_S h\,\rho\,\mathbf{u} = \sum_m \int_{S_m} h\,\rho\,\mathbf{u} \approx \sum_m \left[A_m \sum_{l=w,g} h^l\,\rho^l\,\left(\mathbf{v}^l\right)^{\mathrm{UP}} \right] = \Phi, \tag{28}$$

where A_m is the surface area of the part S_m and UP is denoting the upstream control volume. The capacity term in the equation (10) is a function of temperature. Both the internal energy of the phase u^l and the internal energy of rock u_r in the capacity term are dependent on temperature. The capacity term is treated as

$$\frac{\partial}{\partial t}\int_V \rho\,u \simeq \int_V \frac{\partial}{\partial t}(\rho\,u) \simeq \int_V \beta\,\frac{\partial T}{\partial t}, \tag{29}$$

where β is given as

$$\beta = \sum_{l=w,g} \phi_p\,S^l\,c^l\rho^l + c_r\,\rho_r\,(1-\phi_p), \tag{30}$$

In the above equation, $c^l = \partial u^l/\partial T$ is the specific heat capacity at constant pressure of the phase l and $c_r = \partial u_r/\partial T$ is the specific heat capacity of the rock. For discretization β is approximated by cell center value. After substituting the above terms, the discrete form of energy conservation equation (10)

for a control volume i with volume V and surface S reads as

$$\beta_i \frac{\partial T_i}{\partial t} + \sum_m \xi_{ij}(T_j - T_i) = Q_i - \Phi_i, \tag{31}$$

Backward Euler is used for time discretization. A residual form of the above equation in matrix notation is

$$\mathbf{F}(\mathbf{T}) \equiv \boldsymbol{D}(\mathbf{T}) \left[\frac{\mathbf{T} - \mathbf{T}^n}{\Delta t^n} \right] + \boldsymbol{A}(\mathbf{T})\, \mathbf{T} - \mathbf{b}(\mathbf{T}^n) = 0, \tag{32}$$

where $\Delta t^n = t^{(n+1)} - t^n$, $\boldsymbol{D} = \mathrm{diag}(\beta_i)$, $\boldsymbol{A} = [\xi_{ij}]$ and $\mathbf{b}(\mathbf{T}^n) = (Q_i - \Phi_i)$. The rock temperature is almost constant and both the convection and conduction terms have coefficients which are dominated by the rock temperatures. So, the above equation my be linearized as

$$\boldsymbol{J}^n\, \Delta \mathbf{T}^n = -\mathbf{F}(\mathbf{T}^\mathbf{n}), \tag{33}$$

$$\mathbf{T}^{n+1} = \mathbf{T}^n + \Delta \mathbf{T}^n \quad n = 0, 1, \ldots. \tag{34}$$

Here

$$\boldsymbol{J}^n = \frac{\boldsymbol{D}(\mathbf{T}^n)}{\Delta t^n} + \boldsymbol{A}(\mathbf{T}^n), \tag{35}$$

$$\mathbf{F}(\mathbf{T}^n) = \boldsymbol{A}(\mathbf{T}^n)\, \mathbf{T}^n - \mathbf{b}^n. \tag{36}$$

3.3 Discretization of the Water Pressure Equation

Space discretization of the water pressure equation (8) is done by the Cell Centered Volume Method

$$\delta_{[i]} \frac{\partial P^w_{[i]}}{\partial t} + \sum_{\nu=1}^{nc} \varepsilon_{\nu[i]} \frac{\partial N_{\nu[i]}}{\partial t} = s_{[i]}, \tag{37}$$

where

$$\delta_{[i]} = \left(\frac{\partial R}{\partial P^w} \right)_{[i]} \quad \text{and} \quad \varepsilon_{\nu[i]} = \left(\frac{\partial R}{\partial N_\nu} \right)_{[i]}. \tag{38}$$

In the equation (37), $s_{[i]}$ denotes the right hand side of the equation (8) at the center of the ith cell in the mesh. The molar mass derivative in the equation (37) can be expressed in terms of the water pressure through the molar mass equation (13) using the following expression for the Darcy velocity

$$\mathbf{v}^\mathbf{l} = -\sum_{m=g,w} \boldsymbol{K} \frac{k_r^{lm}}{\mu^m} (\nabla P^m - \gamma^m \nabla d). \tag{39}$$

Here k_r^{lm} is the generalized relative permeability for coupled multiphase flow, $\boldsymbol{K}$ is the absolute permeability tensor, μ^m is the viscosity of the phase m, P^m is the fluid pressure of phase m, γ^m is the specific weight of the phase m and d is the depth. The transmissibility tensors of each chemical component ν are given as

$$\boldsymbol{t}_\nu^m = \sum_{l=w,g} C_\nu^l \, \xi^l \, \boldsymbol{K} \frac{k_r^{lm}}{\mu^m}, \tag{40}$$

The molar mass derivative can be expressed by using equations (39) and (40) as follows

$$\frac{\partial N_\nu}{\partial t} = \int_S \sum_{m=w,g} \boldsymbol{t}_\nu^m \, (\nabla P^m - \gamma^m \, \nabla d) \cdot \hat{\mathbf{n}} + Q_\nu, \tag{41}$$

The water pressure has been chosen as a primary variable, so the CO_2 gas phase pressure is given in terms of the water pressure and the capillary pressure as by equation (9) and part of the conductivity term can be written as

$$\sum_{m=w,g} \boldsymbol{t}_\nu^m \, \nabla P^m = \sum_{m=w,g} \boldsymbol{t}_\nu^m \, \nabla P^w + \boldsymbol{t}_\nu^g \, \nabla P_c^{\,wg}, \tag{42}$$

Substituting equation (42) into the equation (41) results for each control volume i

$$\frac{\partial N_{\nu[i]}}{\partial t} = \sum_j \boldsymbol{t}_{\nu[ij]} \, P_{[j]}^w + \Psi_{\nu[i]}, \tag{43}$$

where

$$\Psi_{\nu[i]} = \sum_j (\boldsymbol{t}_{\nu[ij]}^g \, P_{c[j]}^{wg} - g_{\nu[ij]\, d_{[j]}}) + Q_{\nu[i]}, \tag{44}$$

where j denotes neighbouring control volumes with a common surface, $\boldsymbol{t}_{\nu[ij]} = \sum_m \boldsymbol{t}_{\nu[ij]}^m$ denotes the discrete transmissibilities and $g_{\nu[ij]}$ is the equivalent discrete gravitation. Substituting the molar mass derivative approximation given by equation (43) into the equation (37) finally gives the pressure equation for control volume i

$$\delta_{[i]} \frac{\partial P_{[i]}^w}{\partial t} + \sum_j \alpha_{[ij]} \, P_{[i]}^w = \beta_{[i]}, \tag{45}$$

where

$$\alpha_{[ij]} = \sum_{\nu=1}^{n_c} \varepsilon_{\nu[i]} \, \boldsymbol{t}_{\nu[ij]} \quad \text{and} \quad \beta_{[i]} = s_{[i]} - \sum_{\nu=1}^{n_c} \varepsilon_{\nu[i]} \, \Psi_{\nu[i]}. \tag{46}$$

Using Backward Euler time discretization in equation (45), the resulting water pressure equation in the residual form reads as

$$\mathbf{F}(\mathbf{P}^w) \equiv \boldsymbol{D}(\mathbf{P}^w) \left[\frac{\mathbf{P^w} - \mathbf{P^{wn}}}{\Delta t^n} \right] + \boldsymbol{A}(\mathbf{P}^w) \, \mathbf{P}^w - \mathbf{b}(\mathbf{P}^w) = 0, \tag{47}$$

where $\boldsymbol{D} = \text{diag}(\delta_{[i]})$, $\boldsymbol{A} = \left[\alpha_{[ij]}\right]$ and $\mathbf{b} = (\beta_{[i]})$. The Newton's iteration for the above non-linear residual equation is

$$\boldsymbol{J}^{[k]}\,\Delta\mathbf{P}^{w[k]} = -\mathbf{F}(\mathbf{P}^{w[k]}), \tag{48}$$

$$\mathbf{P}^{w[k+1]} = \mathbf{P}^{w[k]} + \Delta\mathbf{P}^{w[k]} \quad k = 0, 1, \ldots. \tag{49}$$

Here k is the Newton iteration index and $\mathbf{P}^{w[0]} = \mathbf{P}^{w\,n}$. Jacobian and right hand side are given as

$$\boldsymbol{J}^{[k]} = \left(\frac{\partial\mathbf{F}}{\partial\mathbf{P}^{w}}\right) \approx \frac{\boldsymbol{D}^{[k]}}{\Delta t^{n}} + \mathbf{A}^{n}, \tag{50}$$

$$\mathbf{F}(\mathbf{P}^{w[k]}) = \boldsymbol{D}^{[k]}\left[\frac{\mathbf{P}^{w\,[k]} - \mathbf{P}^{w\,n}}{\Delta t^{n}}\right] + \boldsymbol{A}^{n}\,\mathbf{P}^{w[k]} - \mathbf{b}^{n}. \tag{51}$$

In the limit $k \to \infty$, $\mathbf{P}^{w[k]} \to \mathbf{P}^{w\,n+1}$.

The mathematical models (22)-(23), (33)-(34) and (48)-(49) have been implemented in the in-house research simulator named Athena-CO_2 at the University of Bergen. Solution of these equations provide the primary variables temperature (T), water pressure (P^w) and molar masses of components (N_ν).

4 Thermodynamics of Phase Equilibria

Solution of the temperature, pressure, and molar mass conservation equations provide the primary variables water pressure (P^w), temperature (T) and molar masses of each component (N_ν). The secondary variables are: the molar mass of each component in each phase (N_ν^l), molar fraction of each componenet in each phase (C_ν^l), molar density of each phase (ξ^l), volume of each phase (V^l) and saturation of each phase S^l.

Secondary variables should be computed using thermodynamic phase equilibrium constraints. There are two methods for computing the secondary variables. One method is to use the constraint of equal fugasities of components in different phases at equilibrium ($f_\nu^{l_i} = f_\nu^{l_j}$) together with the cubic equation of state. Since such computations need to done for each grid cell in the mesh, it can computationally very expensive. Another approach is based on the binary mixture thermodynamics. All the components in the system are grouped into two groups water group (wg) and carbon group (cg). The water group contains H_2O, NaCl, CO_2, and different minerals, and carbon group contains only CO_2. We assume that the componenets in the two groups can distribute themselves between two phases (liquid and gas phase). This approximation at

any fixed times t, generates for each phase $l = w, g$ the partial derivatives

$$\frac{\partial N_\nu^l}{\partial N_\mu} \quad \nu, \mu = wg, cg. \tag{52}$$

Here N_{wg} denotes the moles of water group and N_{cg} the moles of carbon group. The derivatives given by the above equation depends on the number of phases that are present in a control volume.

4.1 Single Phase System

The single phase generates two cases either pure water phase or pure gas phase.

Assuming only water phase is present

$$N^g = 0 \Rightarrow \quad N^w = N_{wg} + N_{cg}, \quad N_{wg}^w = N_{wg} \quad \text{and} \quad N_{cg}^w = N_{cg}$$

Assuming only gas phase is present

$$N^w = 0 \Rightarrow \quad N^g = N_{wg} + N_{cg}, \quad N_{wg}^g = N_{wg} \quad \text{and} \quad N_{cg}^g = N_{cg}$$

Here we are assuming that there is no water group component in the gas phase, i.e, $N_{wg}^g = 0$. The Jacobian matrix (assuming the condition given by the equation (20)) is the unit matrix, $\boldsymbol{J} = \boldsymbol{I}$.

4.2 Two Phase System

Consider a control volume where both gas and liquid phases are present. The partial derivatives may be expressed in terms of the bubble, $\beta(P^w, T)$, and dew point, $\alpha(P^w, T)$,

$$\beta = \frac{N_{wg}^w}{N^w}, \quad \alpha = \frac{N_{wg}^g}{N^g}, \quad N^w = N_{wg}^w + N_{cg}^w \quad \text{and} \quad N^g = N_{wg}^g + N_{cg}^g, \tag{53}$$

We are assuming that there is no water group in the gas phase so, $N_{wg}^g = 0.0$. The molar fractions of the two groups are defined as

$$z_{wg} = \frac{N_{wg}}{N}, \quad z_{cg} = \frac{N_{cg}}{N} \quad \text{and} \quad N = N_{cg} + N_{wg}, \tag{54}$$

where z_{wg} is the molar fraction of the water group and z_{cg} is the molar fraction of the carbon group. To further simplify the calculations, let us introduce the

molar fraction of the water phase $z^w = N^w/N$. It can be easily shown

$$z_{wg} = \frac{N^w\beta + N^g\alpha}{N}, \quad \frac{N^w}{N} = \frac{(N^w\beta + N^g\alpha)/(N) - \alpha}{\beta - \alpha}, \quad z^w = \frac{z_{wg} - \alpha}{\beta - \alpha}. \quad (55)$$

The quantities of interest can be expressed as

$$N^w_{wg} = \beta N^w, \qquad N^g_{cg} = (1-\alpha)N^g \quad = (1-\alpha)(1-z^w)N, \quad (56)$$
$$N^g_{wg} = \alpha N^g = \alpha(1-z^w)N, \quad N^o_{cg} = (1-\beta)N^o \quad = (1-\beta)z^w N, \quad (57)$$

The partial derivative of the molar fraction of the water group with respect to the number of moles of water and gas group can be expressed as

$$\frac{\partial z_{wg}}{\partial N_{wg}} = \frac{1 - z_{wg}}{N}, \quad \frac{\partial z_{wg}}{\partial N_{cg}} = \frac{-z_{wg}}{N}, \quad (58)$$

Jacobian matrix is defined as

$$\left(\frac{\partial N^w_\nu}{\partial N_\mu}\right) = \begin{bmatrix} \frac{\partial N^w_{wg}}{\partial N_{wg}} & \frac{\partial N^w_{cg}}{\partial N_{wg}} \\ \\ \frac{\partial N^w_{wg}}{\partial N_{cg}} & \frac{\partial N^w_{cg}}{\partial N_{cg}} \end{bmatrix} = \begin{bmatrix} \frac{(1-\alpha)\beta}{\beta-\alpha} & \frac{(1-\alpha)(1-\beta)}{\beta-\alpha} \\ \\ -\frac{\alpha\beta}{\beta-\alpha} & -\frac{\alpha(1-\beta)}{\beta-\alpha} \end{bmatrix}, \quad (59)$$

similarly for the gas phase

$$\left(\frac{\partial N^g_\nu}{\partial N_\mu}\right) = \begin{bmatrix} \frac{\partial N^g_{wg}}{\partial N_{wg}} & \frac{\partial N^g_{cg}}{\partial N_{wg}} \\ \\ \frac{\partial N^g_{wg}}{\partial N_{cg}} & \frac{\partial N^g_{cg}}{\partial N_{cg}} \end{bmatrix} = \begin{bmatrix} -\frac{\alpha(1-\beta)}{\beta-\alpha} & -\frac{(1-\alpha)(1-\beta)}{\beta-\alpha} \\ \\ \frac{\alpha\beta}{\beta-\alpha} & \frac{(1-\alpha)\beta}{\beta-\alpha} \end{bmatrix}. \quad (60)$$

The sum of the above two matrices is equal to an identity matrix.

5 CO_2-Water-Rock Interactions

For solving aqueous species and mineral reactions, we use the ACCRETE package. ACCRETE is an acronym for **A**thena **C**arbon **C**apture and sto**R**age geoch**E**mis**T**ry modul**E**. The ACCRETE module is called as an external object from the Athena code for each control volume and for each timestep. Reactions included are those generally believed to play a significant role during CO_2 storage (see [31]). Interactions between a total of 16 mineral species, 13 aqueous solutes, H_2O solvent and CO_2 as a separate gaseous or supercritical phase are at present being calculated. Thermodynamic data for mineral reactions and aqueous species is calculated by the SUPCRT92 program [32]

using the dprons96.dat database. The standard state adopted in this study is that of unit activity for pure minerals and H_2O at any temperature and pressure. For aqueous species other than H_2O, the standard state is unit activity of the species in a hypothetical 1 molal solution referenced to infinite dilution at any temperature and pressure. For gases, the standard state is for unit fugacity of a hypothetical ideal gas at 1 bar pressure. Equilibrium constants for reactions are calculated from standard state free energies of formation of the constituent components. The temperature dependence of the equilibrium constants is given by a Van't Hoff type of expression neglecting any temperature dependence on the enthalpy. This provides sufficient accuracy since the volumetric effects on the enthalpy is small in the liquid phase. The difference in specific heat capacities across the reaction is more reaction individual but in many cases the effect is negligible relative to other sources of errors. The reaction rate r (mol/s) of mineral reactions are calculated as follows

$$r = k\,A\,(10^{SI} - 1)\,(1 - \frac{V_{\mathrm{CO_2}}}{V_\phi}), \tag{61}$$

where k is the kinetic constant for the reaction, A is reactive surface area, SI is the solubility index. $V_{\mathrm{CO_2}}$ and V_ϕ are volumes of CO_2 and pore space respectively. V_ϕ reduces the reactive surface area proportionally to the amount of immiscible CO_2 that fills the pore space. It follows from expression (61) that no mineral reaction occur in the porespace at full CO_2 saturation. The mineral solver in the ACCRETE code updates chemical components according to

$$\mathbf{X} = \Delta t\,\mathbf{r}\,\boldsymbol{V}, \tag{62}$$

where $\mathbf{X}$ is the aqueous component vector, $\mathbf{r}$ is a 1x16 matrix that contains the rate calculated by expression (61) and $\boldsymbol{V}$ is a 16x15 matrix that contains the stoichiometric number of components for each reaction. Δt is the time step size. The time step is reduced if the calculations results in negative concentrations for any of the aqueous components. For more details on how the geochemical interactions are solved in the ACCRETE code, interested readers are referred to [31]. Initial volume fractions of minerals in sand and clay are taken from [31].

6 Simulator Verification through Test Problem 7

For formal and general definition of the Test Problem 7, we refer to the references [11–16]. This problem is intended to investigate the major physical processes associated with the injection of CO_2 into a layered brine formation. This problem has many similarities with the CO_2 injection project at the Sleipner Vest field in the Norwegian sector of the North Sea such as CO_2 in-

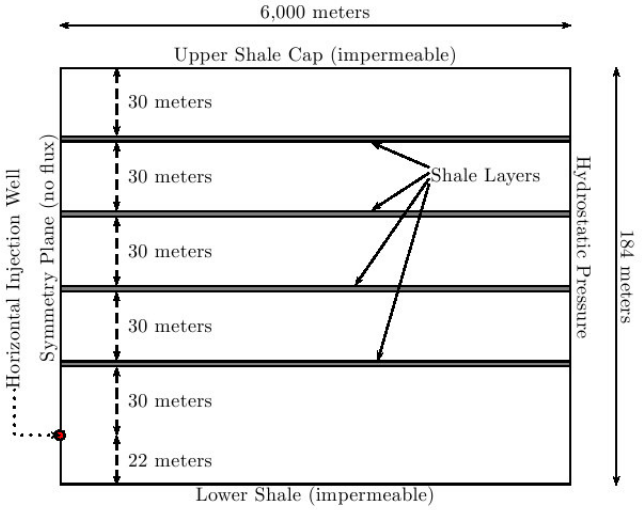

Fig. 1. Schematics of the Test Problem 7 [16].

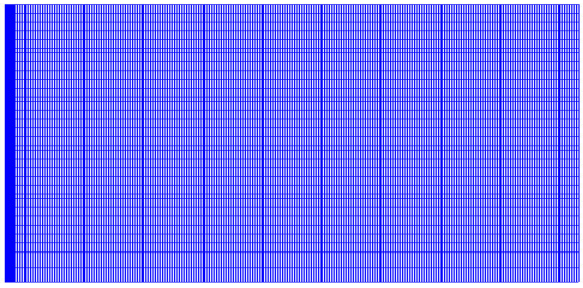

Fig. 2. Mesh for the Test Problem 7.

jection rate of 1.0×10^6 tonnes/year, geometry and medium properties [11–16]. For simplifying the problem several assumption were made such as continuous shale layers, isothermal conditions of 37°C. The Figure 1 is the description of the test problem [16]. It can be seen in the Figure 1 that the formation consists four continuous low permeability shale layers of 3 meters thick. Each shale layer is separated by 30 meters thick sand layer. The thickness of the formation is 184 meters and the injection well is 940 meters below the sea level. Top and bottom surfaces of the formation are impermeable. For meshing domain, we are using our inhouse mesh generator. Figure 2 is the generated mesh in the domain. For capturing the dynamics near the injection point, the mesh is kept very dense near the injection region. Required data for the problem are given in the Table 2.

The Figure 3 is a qualitative comparison of our results 3(a) against the results 3(b) obtained from the report [11]. It is clear from the Figure 3 that our simulator is capturing horizontal and vertical migration of CO_2.

Table 2
Data for the Test Problem 7 [16].

Permeability	Sands: $k = 3 \times 10^{-12} m^2$; Shales: $k = 10^{-14} m^2$
Porosity	Sands: $\Phi = .35$ Shales: $\Phi = 0.1025$
Relative Permeability	
Liquid : Van Genuchten	
$k_{rl} = \sqrt{S^*}\left[1 - \left(1 - [S^*]^{(1/m)}\right)^m\right]^2$	$S^* = (S_l - S_{lr})/(1 - S_{lr})$
irreducible water saturation	$S_{lr} = 0.20$
exponent	$m = 0.40$
Gas : Van Genuchten	
$k_{rg} = \sqrt{S_g^*}\left[1 - \left(1 - \left[S_g^*\right]^{(1/m)}\right)^m\right]^2$	$S_g^* = (S - S_{gr})/(1 - S_{gr})$
irreducible gas saturation	$S_{gr} = 0.05$
exponent	$m = 0.40$
Capillary Pressure	
Van Genuchten	
$P_{cap} = -P_0\left([S^*]^{-1/m} - 1\right)^{1-m}$	$S^* = (S_l - S_{lr})/(1 - S_{lr})$
irreducible water saturation	$S_{lr} = 0.20$
exponent	$m = 0.400$
strength coefficient	Sand: $P_0 = 3.58$ kPa ; Shale: $P_0 = 62.0$ kPa
Initial Conditions	
Salinity	3.2-%
Pressure	Hydrostatic
Temperature	37°C
Injection (Constant rate)	0.1585 kg/s

7 Results and Discussion

7.1 Simulation Setup

The simulation setup is shown in the Figure 4. Our domain is the Utsira formation at the Sleipner Vest field in the Norwegian sector of the North Sea

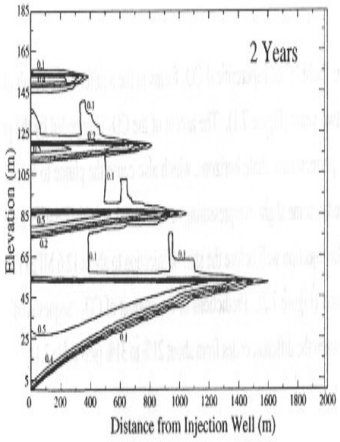

(a) Migration of CO_2 by other simulators [9].

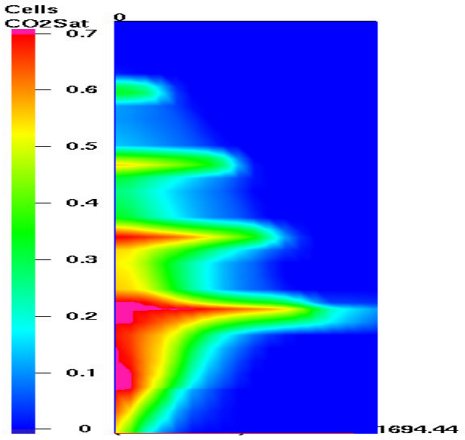

(b) Migration of CO_2 by the Athena.

Fig. 3. Test Problem 7. CO_2 saturation distribution after 2 years.

[17]. The injection point is approximately 1000 m below the sea-level. At this depth, approximate value of hydrostatic pressure and temperature are 110 bar and 37 °C. We are simulating a total volume of $3000 \times 3000 \times 200$ m^3. The formation is highly elonglated. It extend for more than 400 km from north to south and between 50 and 100 km from east to west. It has an estimated area of about 26,100 km^2. The total estimated pore volume of the Utsira formation is about 6.0×10^{11} m^3. CO_2 is injected in the central lowermost grid (see the Figure 4). CO_2 is injected at a rate of 1,000,000 tonnes per year for the first 20 years of simulation. Our injection rate (cf. [1]) and injection period (cf. [2]) are close to the reality at the Sleipner injection site. We simulate 20 years of CO_2 injection followed by 980 years of post-injection. The post-injection period involve interactions between CO_2, formation waters and minerals. The data for this simulation are the same as for the Test Problem No. 7 (see the Table 2).

Seismic profiles [1] and well logs [21] suggest that the Utsira formation contains clayey layers. Based on the rapid upward migration of CO_2 and low permeable nature of clayey layers, seismic profiling also suggest discontinuities in the clayey layers. To take into account these features, we have included five sand units separated by four discontinuous low-permeable clayey layers (see the Figure 4). The discontinuities are added in an XZ plane (CO_2 injection plane) to the clayey layers by inserting grids with sand properties (see the Figure 4).

Topography of the top (XY) Utsira surface is provided by Statoil in the form of seismic data. Seismic profiles [1] shows that the clayey layers follow the topography of the top surface. Based on this information, we meshed a $3000 \times 3000 \times 200$ m^3 of the formation into $9 \times 9 \times 24$ hexahedral elements. It can

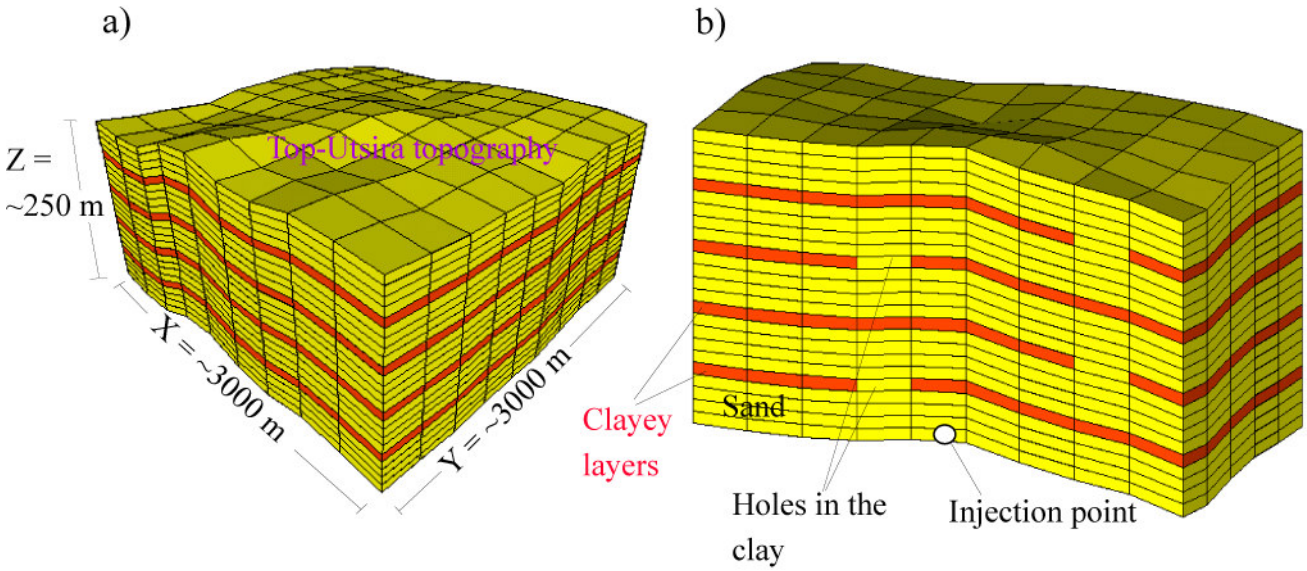

Fig. 4. Simulation setup. Meshed Utsira formation at the Sleipner injection site. (a) The total volume of the meshed area is $3000 \times 3000 \times 200$ m^3. (b) A cutplane section (XZ) showing the injection point and sandy units separated by discontinuous clayey horizons.

be seen in the Figure 4, five sand units and four low-permeable clayey layers follow the topography of the top surface. For grid generation, we are using an in-house grid generation package called the RMS-GG.

We are simulating two scenarios. In the first simulation, hydrostatic pressure is specified at the four sides, and in the second simulation a constant flux is specified at the left boundary and keeping hydrostatic pressure at the remaining three sides.

7.2 Evolution of CO_2 Immiscible Saturation in the Utsira Sand

Mobility of immiscible CO_2 is of major importance for evaluating the risk of leakage. During and after the injection of CO_2, some of the CO_2 can dissolve in the formation water, some can react with the present minerals and some of the CO_2 can exists as a separate phase (immiscible). Immiscible CO_2 may be mobilized due to buoyancy forces. Amount of CO_2 dissolved at a given time is mainly determined by temperature of the formation, pressure of the formation, salinity of the aqueous phase, contact of immiscible CO_2 with undersaturated water and mobility of immiscible CO_2. Mineral reactions that consume CO_2 from the aqueous solution, as is the case for solid carbonate precipitation, consume immiscible CO_2 indirectly through the water phase. The immiscible

CO_2 is trapped in lowpermeable domal structures or other structural traps or alternatively spills out and migrate further towards the surface.

Figures 6, 7, 8, 9 and 10 present temporal evolution of immiscible CO_2 in the absence of regional flow at the time 1, 2, 30, 500 and 1000 years (see Figure 5 for scale). As can be seen in the snapshots, immiscible CO_2 spreads as a continuous stream from the injector and up to the top of the formation. The injection rate is higher than the rate of dissolution of CO_2 in the aqueous phase. During this time, both the saturation and spatial extension of immisible CO_2 increase. Preferred path of immiscible CO_2 stream is through the holes in the clayey layers. It can also be notice that a good amount of CO_2 is also retained in structural highs in the clay horizons. During the post-injection period (CO_2 injection stops at 20 years), CO_2 continues to migrate upwards and also dissolve in the aqueous solution. During the first 480 years of post-injection period (see the Figure 9 for the time 500 years), most immiscible CO_2 is trapped in topographic highs at the top of the formation. Some minor amount of immiscible CO_2 is still trapped by the uppermost clay horizons. During the next 500 years, we saw little change in the immiscible CO_2 with respect to saturation of the immiscible CO_2 and spatial extension. This observation suggests that formation water in the vicinity of immiscible CO_2 is close to saturation after 500 years. This is further confirmed by the pH changes with times.

7.3 Temporal and Spatial evolution of pH at the Utsira Formation

CO_2 injection significantly affects pore water chemistry. It drops the pH which further enhances formation and dissociation of carbonic acid. Drop in the pH is partly buffered by mineral reactions and especially by the carbonates that are present in the reservoir prior to injection. The resulting pH is instrumental in the reactivity of the reservoir minerals during CO_2 injection. Figures 12, 13, 14, 15 and 16 illustrate the temporal and spatial evolution of pH (see Figure 11 for scale). Each time t is illustrated with an isovolume that locates the most affected parts of the system. By comparing pH evolution with the CO_2 flow presented in the previous section, we see that the two are clearly related. Areas around the immiscible flow where CO_2 dissolves to saturation show the largest decrease in pH. At the time 2 years, and 30 years, a zone of low pH spreads around the injector and up to the top of the formation.

The lowest pH values are in the central part where it drops rapidly from initial 7.0 to around 4.9. This value is at full CO_2 water saturation equilibrated with calcite that are present in both the sand and clayey layers. As the time proceeds, more and more of the system is affected by CO_2 dissolution and the whole system approaches a pH of around 5.0. At 30 years the pH drop is seen

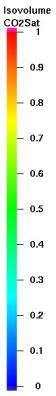

Fig. 5.

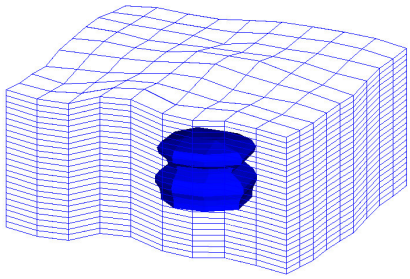

Fig. 6. CO_2 immiscible saturation at 1 year.

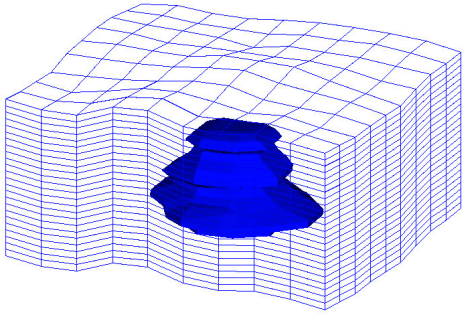

Fig. 7. CO_2 immiscible saturation at 2 years.

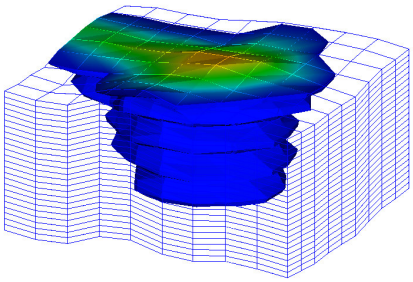

Fig. 8. CO_2 immiscible saturation at 30 years.

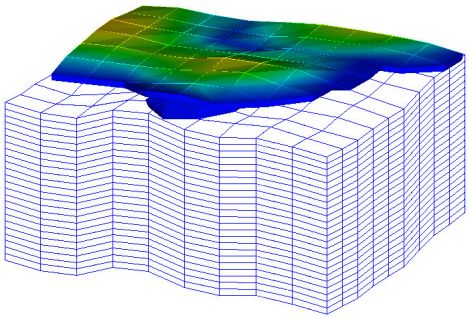

Fig. 9. CO_2 immiscible saturation at 500 years.

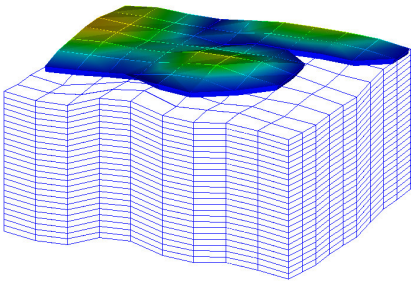

Fig. 10. CO_2 immiscible saturation at 1000 years.

to be strongly asymmetric in the system. This is caused by preferential CO_2 flow and dissolution to the highest topographies beneath clayey horizons and the top of the formation as seen in the Figure 15. The upper left corner of the system shows such a topographic low. The pH in this region stays largely unaffected by the CO_2 injection; i.e., pH higher than 5.5, for more than 500 years. At 1000 years (end of the simulation), the pH of this area also drops below 5.5 and approaches the values of the remaining sands. The evolution of acidity from 500 to 1000 years proceeds towards a uniform low value. The high

Fig. 11.

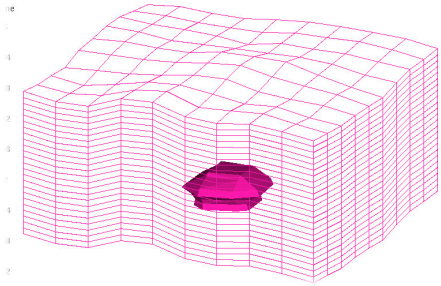

Fig. 12. Isovolume of pH at 1 year.

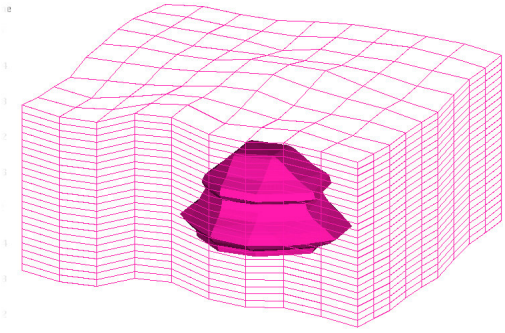

Fig. 13. Isovolume of pH at 2 years.

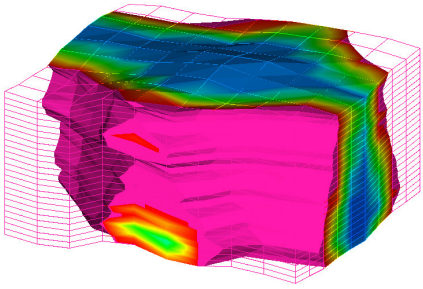

Fig. 14. Isovolume of pH at 30 years.

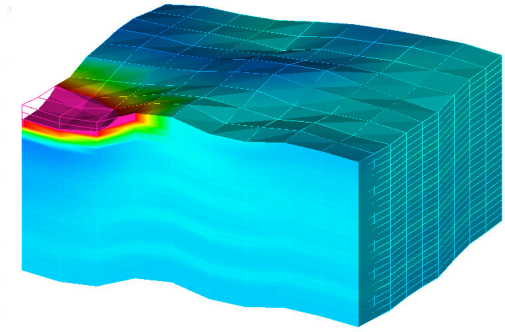

Fig. 15. Isovolume of pH at 500 years.

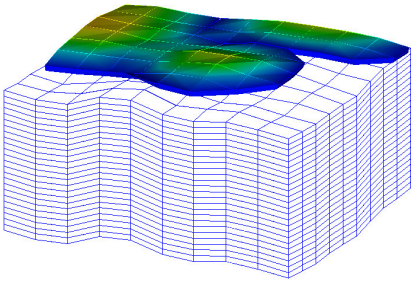

Fig. 16. Isovolume of pH at 1000 years.

resolution of pH in the isovolumes shows that after the rapid initial drop in pH to approximately 4.9, slow mineral reactions change the pH to approximately 5.0. At 1000 years the pH of the clayey layers are uniformly at a slightly higher pH than the sands. A detailed description of mineral reactions and simulations is given in our article [33].

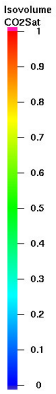

Fig. 17.

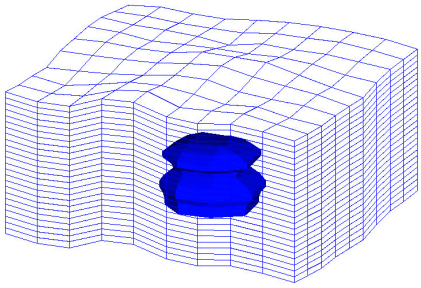

Fig. 18. Isovolume of immiscible CO_2 at 1 year.

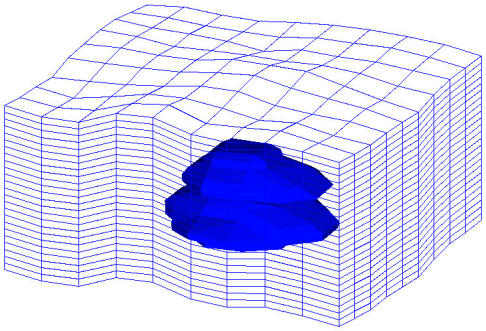

Fig. 19. Isovolume of immiscible CO_2 at 2 years.

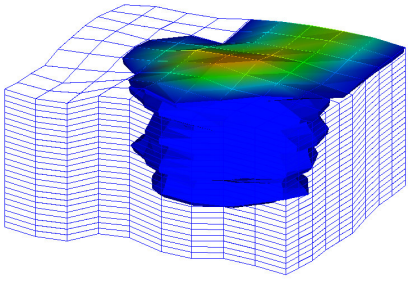

Fig. 20. Isovolume of immiscible CO_2 at 30 years.

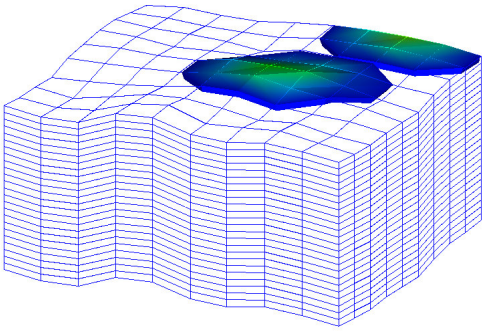

Fig. 21. Isovolume of immiscible CO_2 at 500 years.

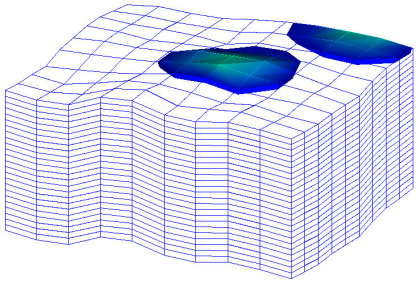

Fig. 22. Isovolume of immiscible CO_2 at 1000 years.

7.4 Effects of a regional formation water flow

We have seen in previous sections that the buoyant flow of immiscible CO_2 migrates to topographic highs beneath low-permeable clayey or shale layers and beneath the top seal. After some time most of the formation water is saturated with CO_2 and the immiscible phase reaches a steady state at topographic highs. We have also seen how the spatial distribution of CO_2 in

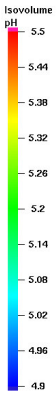

Fig. 23.

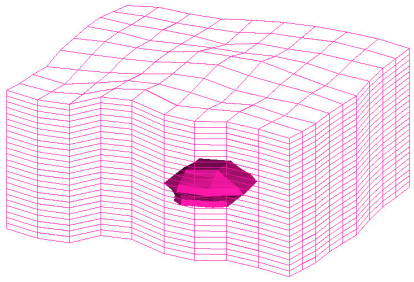

Fig. 24. Isovolume of pH at 1 year.

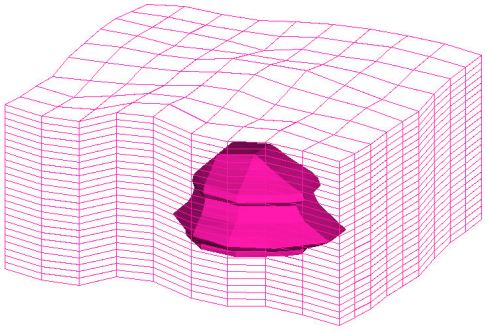

Fig. 25. Isovolume of pH at 2 years.

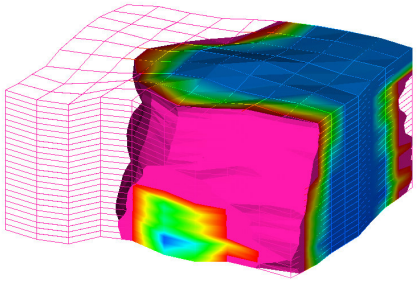

Fig. 26. Isovolume of immiscible CO_2 at 30 years.

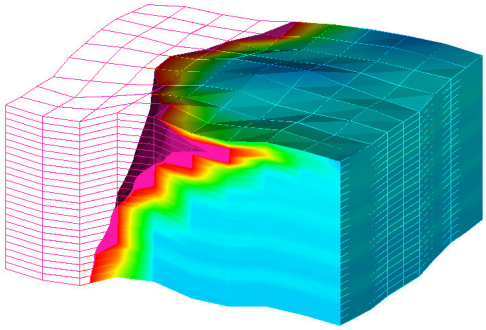

Fig. 27. Isovolume of pH at 500 years.

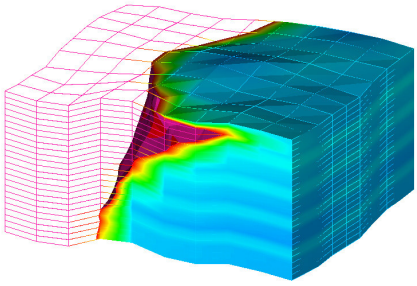

Fig. 28. Isovolume of pH at 1000 years.

the formation is instrumental in defining the pH. In this section, we present a simulation using the same system definition as in the previous simulation (see the Figure 4), but with a regional flow of formation water of approximately 1 m/y perpendicular to the YZ plane. Figure 29 shows snapshots of water flow at 100 years of simulation of two sections XZ and XY which are parallel to the regional flow. The figure suggests that the regional flow leads to an average direction of the flow through the system but that stagnant zones occur locally.

We illustrate the reactivity of the system by presenting the spatial evolution

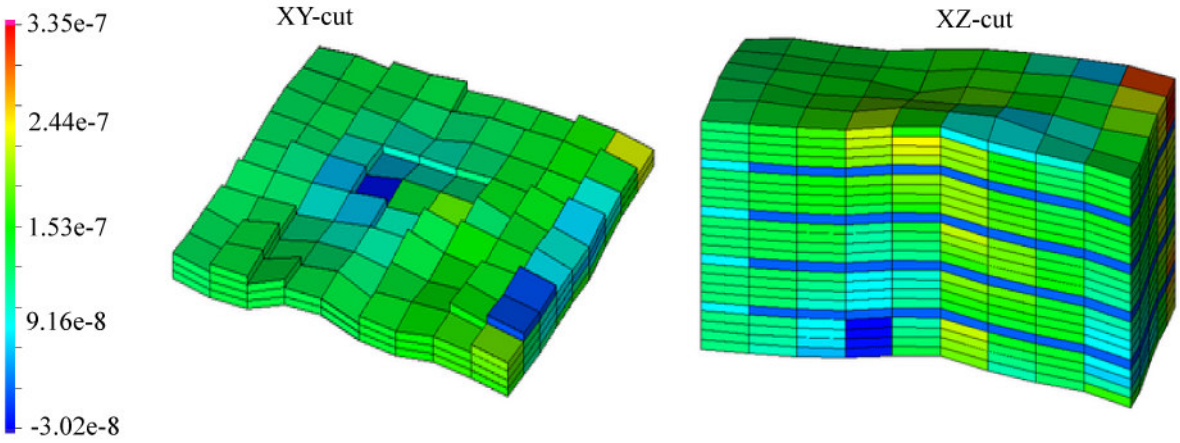

Fig. 29. Flowfield through the simulated volume in a lower XY surface beneath the lowermost clayey horizon and a profile through the central XZ cutplane.

of the CO_2 immiscible phase (see the Figures 18, 19, 20, 21 and 22. Figure 17 shows the scale) and the pH evolution (see the Figures 24, 25, 26, 27 and 28. Figure 23 shows the scale). The range of CO_2 immiscible saturation and the pH are 0.1 to 1.0 and 4.9 to 5.5, respectively for the isovolumes (as for the previous simulation). During the first 2 years (injection period is 20 years) the plume of immiscible CO_2 looks much the same as for the stagnant case (no flow). The same is the case for the pH evolution. Both pH and CO_2 saturations are however more asymmetric and shifted slightly more to the righthand side of the system. After 30 years of simulation, the effect of the flow is much more evident. The immiscible CO_2 and acidified formation waters now principally occupy the righthand half of the system, whereas the left-hand half is largely unaffected by the injection. During the next 970 years most of the immiscible CO_2 is dissolved in the formation water and the pH approach a value of approximately 5 (buffered by mineral reactions). Two features are worth noting from these simulations. First, more CO_2 is dissolved when having a regional flow through the system (flow refreshes the formation waters in contact with the CO_2 phase). Second, a regional flow of 1 m/y has a dramatic effect on the immiscible CO_2 when it accumulates beneath the topographic highs.

The capillary presure curves, used in the Test Problem No. 7 [16] and therefore also used in our simulation, represent an imbibition displacement process. As the Utsira rock may be water-wet, one should instead have used the capillary drainage curves for the lithologies. Depending on the size of the threshold pressure for the shaley layers the vertical migration of CO_2 will then be slowed down. The possibility of hydrodynamic trapping below the shale will then increase and so will also the contact surface between the fluid phases. This is a very important parametre for the chemical and mineral reaction processes.

8 Conclusions

The mathematical models and their discretization for capturing dynamics of CO_2 in porous medium are presented. These models have been implemented in the inhouse research simulator named Athena-CO_2. We have simulated approximately 2.25 km^3 volume of the Utsira Sand around the CO_2 injector at the Sleipner in the presence and absence of regional flow. As CO_2 is injected, immiscible CO_2 rises buoyantly. It accumulates beneath low-permeable intraformation clayey horizons and also beneath the top of the formation in topographic highs. Dissolution of CO_2 in the formation water decreases the pH to around 5.0 in equilibrium with calcite. The fast calcite reaction is considered as instrumental in buffering pH drop during CO_2 storage. So, it should be included as an equilibrium reaction if it is likely to be present in a system, even if the slower mineral reactions are considered non-significant. Acidic environment induces dissolution of primary minerals such as Clinochlore-14A, Daphnite-14A and Annite which mainly precipitate Magnesite and Siderite. Dawsonite precipitates only as a minor phase and dissolves at later stages of the simulations. Because of large timesteps in the mineral solver of the ACCRETE code, the present study provide a conservative estimate of the minerals' reactivity. Since, laboratory rates used in the ACCRETE is known to overestimate reaction kinetics compared to natural systems. So, error induced due to large time steps is regarded as acceptable. Our second simulation which involve regional flow of 1 m/y shows that regional flow strongly affects CO_2 dynamics such as spatial distribution of immiscible CO_2. Regional flow enhances dissolution of CO_2 into the aqueous phase. It is observed that a regional flow can force the CO_2 to leave the system. It can extensively pollute downstream areas.

In the present study, we are simulating a small region around the injection well (2.25 km^3). Size of the Utsira formation compared to this region is very large. In future, we plan to simulate full Utsira formation.

For visualization, we are using the Graphical Mesh Viewer (GMV). GMV was developed at the Los Alamos National Laboratory. Plotting of isovolumes and cutplanes proved very valuable in presenting our 3-D simulations. See the GMV manual at http://www-xdiv.lanl.gov/XCM/gmv/doc.color.pdf for more detailes on the software.

9 Acknowledgement

This work is supported by the Research Council of Norway and the Norsk Hydro through the Grant 151400/210 to the University of Bergen, Norway.

References

[1] R. Korbol and A. Kaddour. Sleipner Vest CO_2 Disposal - Injection of Removed CO_2 into the Utsira Formation, *Energy Convers. Mgmt.*, **36**, 509 - 512, 1995.

[2] R. A. Chadwick, P. Zweigel, U. Gregersen, G. A. Kirby, S. Holloway and P. N. Johannessen. Geological reservoir characterization of a CO2 storage site: The Utsira Sand, Sleipner, northern North Sea, *Energy Elsevier*, **29**, 1371-1381, 2004.

[3] I. Garrido, G. E. Fladmark, and M. Espedal. An improved numerical simulator for multiphase flow in porous media. *Internat. J. Numer. Methods Fluids*, **44(4)**, 447–461, 2004.

[4] I. Garrido, E. Øian, M. Chaib, G. E. Fladmark, and M. S. Espedal. Implicit treatment of compositional flow. *Comput. Geosci.*, **8(1)**, 1–19, 2004.

[5] K. J. Hersvik and M. S. Espedal. Adaptive hierarchical upscaling of flow in heterogeneous reservoirs based on an a posteriori error estimate. *Comput. Geosci.*, **2(4)**, 311–336, 1999.

[6] H. Reme, M. S. Espedal and G. E. Fladmark. A preconditioning technique as an upscaling procedure. In *Resource recovery, confinement, and remediation of environmental hazards (Minneapolis, MN, 2000)*, volume 131 of *IMA Vol. Math. Appl.*, pages 283–296. Springer, New York, 2002.

[7] H. Reme, G. Øye, M. S. Espedal and G. E. Fladmark. Parallelization of a compositional reservoir simulator. In *Numerical treatment of multiphase flows in porous media (Beijing, 1999)*, volume 552 of *Lecture Notes in Phys.*, pages 244–266. Springer, Berlin, 2000.

[8] M. Chaib. Implcit Molar Mass Formulations in Secondary Oil Migration. *PhD Thesis. The University of Bergen, Norway*, 2002.

[9] G.E. Fladmark. The Volume Balancs Method applied to a 4-Phase Problem. *Lecture Notes. The University of Bergen, Norway*, 1994.

[10] T. W. Wong, A. Firoozabadi and K. Aziz. The Relationship of the Volume Balancs Method of Compositional Simulation to the Newton-Raphson Method, SPE Reservoir Structure Symposium, **5**, 414-422, 1990.

[11] K. Pruess, J. E. Garcia, T. Kovscek, C. Oldenburg, J. Rutqvist, C. Steefel. Intercomparison of Numerical Codes for Geologic Disposal of CO_2. *Technical Report LBNL-51813, Lawrence Berkeley National Laboratory, Berkely, CA.*, 2000.

[12] K. Pruess and J. E. Garcia. Solutions of Test Problems for Disposal of CO_2 in Saline Aquifers. *Technical Report LBNL-51812*, 2002.

[13] Xu. Tianfu, A. John, K. Pruess. Numerical Simulation of CO_2 Disposal by Mineral Trapping in Deep Aquifers, *Applied Geochemistry*, **19**, 917-936, 2004.

[14] Xu. Tianfu, A. John, K. Pruess. Reactive Geochemical Transport Simulation to Study Mineral Trapping for CO_2 Disposal in Deep Arenaceous Formations. *Journal of Geophysical Research*, **108**, 2003.

[15] K. Pruess, J. E. Garcia, T. Kovscek, C. Oldenburg, J. Rutqvist, C. Steefel, Xu. Tianfu. Code Intercomparison Builds Confidence in Numerical Simulation Models for Geologic Disposal of CO_2. *Energy*, **29**, 1431-1444, 2004.

[16] J. E. Garcia. Fluid Dynamics of Carbon Dioxide Disposal into Saline Aquifers. *PhD Thesis, The University of California, Berkeley*, 2003.

[17] E. Lindberg, P. Zweigel, P. Bergmo, A. Ghaderi and A. Lothe. Prediction of CO_2 Distribution Pattern Improved by Geologic and Reservoir Simulation and Verified by Time Lapse Seismic. Proceedings, 5th International Conference on Greenhouse GAS Control Technologies. CISRO Publ. Collingwood, VIC, Australis, 372-377, (2001).

[18] R. Arts, O. Eiken, A. Chadwick, P. Zweigel, L. van der Meer and B. Zinszner. Monitoring of CO2 Injected at Sleipner Using Time Lapse Seismic Data. Abstracts of the 6th International conference on Greenhouse Gas Control Technology (GHGT-6), Kyoto, Japan, 1-4 October 2002

[19] P. Zweigel, M. Hamborg, R. Arts, A. Lothe, and A. & Tmmers. Prediction of migration of CO_2 injected into an underground depository: Reservoir geology and migration modelling in the sleipner case (north sea). *5th International Conference on Greenhouse Gas Control Technologies, Cairns (Australia)*, August, 2000.

[20] J. Gale. Overview of CO_2 emission sources, potential, transport and geological distribution of storage possibilities. *IPCC Workshop on Carbon Dioxide Capture and Storage*, **1**, 1990.

[21] U. Gregersen, O. Michelsen and J. C. Søresnsen. Stratigraphy and facies distribution of the Utsira Formation and the Pliocence sequences in the northern North Sea. *Marine and Petroleum Geology*, **14**, 893–914, 1997.

[22] R. A. Chadwick, S. Holloway, G. A. Kirby, U. Gregersen and P.N. Johannessen. The Utsira Sand, Central North Sea - An assessment of its potential for regional CO2 disposal. *5th International Conference on Greenhouse Gas Control Technologies*, Cairns (Australia), August 2000.

[23] A. Baklid, R. Korbl and G. Owren. Sleipner Vest CO_2 disposal, CO_2 injection into a shallow underground aquifer. *Paper presented on the 1996 Society of Petroleum Engineers Annual technical Conference and Exhibition*, Denver, Colorado, USA, SPE paper 36600, 1-9, 1996.

[24] I. Aavatsmark. An introduction to multipoint flux approximations for quadrilateral grids. *Comput. Geosci.*, 6(3-4):405–432, 2002.

[25] J. W. Watts. A compositional formulation of the pressure and saturation equations. *Society of Petroleum Engineers*, 341–354, 1991.

[26] G. Qin, H. Wang, R. E. Ewing, and M. S. Espedal. Numerical simulation of compositional fluid flow in porous media. In *Numerical treatment of multiphase flows in porous media (Beijing, 1999)*, volume 552 of *Lecture Notes in Phys.*, pages 232–243. Springer, Berlin, 2000.

[27] M. S. Espedal and K. H. Karlsen. Numerical solution of reservoir flow models based on large time step operator splitting algorithms. In *Filtration in porous media and industrial application (Cetraro, 1998)*, volume 1734 of *Lecture Notes in Math.*, pages 9–77. Springer, Berlin, 2000.

[28] M. S. Espedal, A. Fasano, and A. Mikelić. Filtration in porous media and industrial application, volume 1734 of *Lecture Notes in Mathematics*. Springer-Verlag, Berlin, 2000. Lectures from the 4th C.I.M.E. Session held in Cetraro, August 24–29, 1998, Edited by Fasano, Fondazione C.I.M.E. [C.I.M.E. Foundation].

[29] G. E. Fladmark. Secondary Oil Migration. Mathematical and Numerical Modelling in SOM Simulator. *Tech. Rep. , Norks Hydro ASA, E & P Research Center, Bergen, Norway*, 1997.

[30] G. E. Fladmark. Athena as a Thermal Mass Flow and Solid Mechanics Simulator. *Lecture Notes, The University of Bergen, Norway*, May, 2005.

[31] H. Hellevang and B. Kvamme. CO_2 - water-rock interactions - ACCRETE simulations of geological storage of CO_2, *Submitted to Appl. Geoch.*, 2005.

[32] J. W. Johnson, E. H. Oelkers and H. C. Helgeson. SUPCRT92: A Software Package for Calculating the Standard Molal Thermodynamic Properties of Minerals, Gases, Aqueous Species, and Reactions from 1 to 5000 bar and 0 to 1000°C, *Computers and Geosciences*, **18**, 7, 899- 947, 1992.

[33] H. Hellevang, S. K. Khattri, G. E. Fladmark and B. Kvamme. CO_2 storage in the Utsira Formation: ATHENA 3-D reactive transport simulations, *Submitted to the journal of Basin Research,* 2005.